RESEARCH ARTICLE | DECEMBER 11 2023

Near-field thermal emission from metasurfaces constructed of SiC ellipsoidal particles \bigcirc

Lindsay P. Walter ■ [0]; Joseph C. McKay [0]; Bart Raeymaekers [0]; Mathieu Francoeur ■ [0]



J. Appl. Phys. 134, 225102 (2023) https://doi.org/10.1063/5.0164073





CrossMark





9 December 2023 17:12:31

Near-field thermal emission from metasurfaces constructed of SiC ellipsoidal particles

Cite as: J. Appl. Phys. **134**, 225102 (2023); doi: 10.1063/5.0164073

Submitted: 13 July 2023 · Accepted: 14 November 2023 ·

Published Online: 11 December 2023







Lindsay P. Walter, 1,a) (D) Joseph C. McKay, 1 (D) Bart Raeymaekers, 2 (D) and Mathieu Francoeur 3,a) (D)

AFFILIATIONS

- Radiative Energy Transfer Lab, Department of Mechanical Engineering, University of Utah, Salt Lake City, Utah 84112, USA
- ²Manufacturing and Tribology Laboratory, Department of Mechanical Engineering, Virginia Tech, Blacksburg, Virginia 24061, USA
- ³Radiative Transfer Lab, Department of Mechanical Engineering, McGill University, Montréal, Quebec H3A 0C3, Canada

ABSTRACT

We model near-field thermal emission from metasurfaces structured as two-dimensional arrays of ellipsoidal SiC particles. The modeling approach is developed from fluctuational electrodynamics and is applicable to systems of ellipsoidal particles within the dipole limit. In all simulations, the radial lengths of particles are restricted to the range of 10–100 nm, and interparticle spacing is constrained to at least three times the particle characteristic length. The orientation and dimensions of constituent ellipsoidal particles are varied to tune localized surface phonon resonances and control the near-field energy density above metasurfaces. Results show that particle orientation can be used to regulate the relative magnitude of resonances in the energy density, and particle dimensions may be changed to adjust the frequency of these resonances within the Reststrahlen band. Metasurfaces constructed from particles with randomized dimensions display comparatively broadband thermal emission rather than the three distinct resonances seen in metasurfaces made with ellipsoidal particles of equivalent dimensions. When the interparticle spacing in a metasurface exceeds about three times the particle characteristic length, the spectral energy density above the metasurface is dominated by individual particle self-interaction and can be approximated as a linear combination of single-particle spectra. When interparticle spacing is at the lower limit of three times the characteristic length, however, multiparticle interaction effects increase and the spectral energy density above a metasurface deviates from that of single particles. This work provides guidance for designing all-dielectric, particle-based metasurfaces with desired near-field thermal emission spectra, such as thermal switches.

Published under an exclusive license by AIP Publishing. https://doi.org/10.1063/5.0164073

I. INTRODUCTION

Metamaterials are engineered materials composed of structures much smaller than the operational electromagnetic wavelength and display properties unique from those of their constituent materials. In thermal applications, metamaterials have been designed to tune the spectrum²⁻⁴ and direction⁵⁻⁸ of thermal emission for desired functionalities. For example, thermal metamaterials have been designed for both fixed and dynamic emissivity regulation in daytime radiative cooling applications, ⁹⁻¹³ to increase the efficiency of thermophotovoltaic devices through selective-wavelength emitter design, ¹⁴⁻¹⁷ as a thermal lens for focused heating over a delimited spot, ¹⁸ and for thermal camouflage materials. ¹⁹⁻²² To achieve such a broad range of functionalities, researchers have worked to develop efficient methods and strategies for metamaterial design. ²³⁻²⁵

For full characterization and informed design of metamaterials across length scales, it is important to resolve thermal radiation in

the near field.²⁶ Overwhelmingly, researchers have focused on modeling near-field thermal radiation from metamaterials structured as one- and two-dimensional gratings composed of plasmonic materials, such as metals and doped semiconductors.^{27–35} However, the design space of grating structures is somewhat limited (i.e., tuning thermal radiation is restricted to material modification and adjustments of grating size parameters). In order to realize a diverse set of functionalities, alternative metamaterial designs are required.

One metamaterial structure that has shown promising thermal behavior is the particle-based structure. Researchers have found that particle-based metamaterials can support collective lattice resonances that affect thermal emission and can display enhanced heat flux in the near field due to excitation of localized surface modes. Localized surface modes do not exist in bulk materials and are affected by particle geometry and interparticle

^{a)}Authors to whom correspondence should be addressed: L.Walter@utah.edu and mathieu.francoeur@mcgill.ca

interactions. In all-dielectric, particle-based metamaterials, localized surface phonons (LSPhs) can be the dominant mode of near-field thermal emission, 42 thereby providing an opportunity to tune thermal emission through geometric modification of the metamaterial structure. Such particle-based metamaterials could be manufactured via ultrasound-directed self-assembly, which allows three-dimensional control over the spatial organization of the particles dispersed in a macroscale volume.4

To handle the scale of particle-based metamaterials, near-field thermal radiation models must support large numbers of particles. Since fluctuational electrodynamics models of near-field thermal radiation are often computationally intractable for metamaterials made of many unique, complex-shaped particles, simplified dipole approximations have been developed to reduce computational costs in particle-based designs. 46-48 Researchers have employed these dipole approximations to model near-field thermal radiation in systems of many particles arranged in random clusters, 49 in ordered particle arrays, 50-53 and in fractal formations. 54 Thus far, however, models between large groups of particles have been restricted to spherical dipoles. Some researchers have modeled near-field radiative heat transfer between nonspherical dipoles, such as spheroids, 55-57 but these analyses have been limited to systems of three or fewer particles. To innovate new particle-based metamaterial designs, dipole models must accurately reflect the particle distributions and geometric irregularities in real, manufactured metamaterials. Development of nonspherical dipole models for near-field thermal radiation between large numbers of particles would help to realize this outcome.

In this article, we address this knowledge gap by presenting a model of near-field thermal emission from dielectric-based metasurfaces constructed of ellipsoidal particles. By focusing on ellipsoidal particles, we can control the geometry of particles along three separate axes, thereby broadening the scope of what types of particles may be modeled, from needle-like structures to asymmetric flat disks and beyond. Here, metasurfaces are composed of a single layer of ellipsoidal SiC particles with radii between 10 and 100 nm. Interparticle spacing is at least three times the particle characteristic length, a regime in which the accuracy of dipole approximations is deemed acceptable. 48 We vary the particle dimensions and orientation and analyze the resulting near-field thermal emission as characterized by the spectral near-field energy density. Near-field energy density is modeled using a variation of the discrete system Green's function method^{58,59} where ellipsoidal geometry is accounted for in the self-interaction term of the free-space Green's function. We find that the proper choice of geometric parameters (e.g., dimensions, orientation) of the constituent ellipsoidal particles allows for spectral control and tunability of near-field thermal emission from a metasurface. In particular, the particle dimensions can be used to control the location and bandwidth of localized LSPh resonances that contribute to thermal emission within the Reststrahlen band.

II. METHODS

A. Dipole approximation

We implement an extension of the many-body theory of nearfield radiative heat transfer 47,50,60,61 derived within the framework

of the discrete system Green's function method^{58,59} to calculate the energy density above metasurfaces composed of ellipsoidal particles in the dipole limit. For application of dipole approximations, we require two constraints: first, the characteristic length of the particles must be smaller than the thermal wavelength defined by Wien's law (i.e., $L_{\rm ch} \ll \lambda_T = 2898/T \,\mu{\rm m\,K}$), and, second, the center-of-mass separation distance between particles must be at least three times the characteristic length of the particles (i.e., $d \gtrsim 3L_{\rm ch}$). For ellipsoidal particles, the characteristic length is defined as the maximum of the three ellipsoid semiaxes, $L_{\rm ch} = \max(\{a, b, c\})$. The three ellipsoid semiaxes a, b, and c are given as aligned with the x-, y-, and z-axes of the local Cartesian coordinate system such that the equation for the ellipsoid quadratic surface may be written as $\frac{x^2}{a^2} + \frac{y^2}{b^2} + \frac{z^2}{c^2} = 1$. In this work, the semi-axes are defined as a < b < c.

B. Fluctuational electrodynamics description of thermal emission

For a system of thermal objects in a nonabsorbing background reference medium, the thermally generated electric field at location r is defined as

$$\mathbf{E}(\mathbf{r},\omega) = i\omega\mu_0 \int_V \overline{\overline{\mathbf{G}}}(\mathbf{r},\mathbf{r}',\omega) \mathbf{J}^{(\mathrm{eq})}(\mathbf{r}',\omega) d^3\mathbf{r}', \quad \mathbf{r} \in \mathbb{R}^3, \quad (1)$$

where $i = \sqrt{-1}$, ω is the angular frequency, μ_0 is the vacuum permeability, $\overline{\overline{G}}(\mathbf{r}, \mathbf{r}', \omega)$ is the system Green's function, $\mathbf{J}^{(eq)}(\mathbf{r}', \omega)$ is the equivalent electric current density, and integration is taken over the three-dimensional space V occupied by all thermal objects and the three-dimensional space V occupied by all thermal objects and the background reference medium. The equivalent electric current density is defined as density is defined as

$$\mathbf{J}^{(\mathrm{eq})}(\mathbf{r}',\omega) = \begin{cases} 0, & \mathbf{r}' \in V_{\mathrm{ref}}, \\ \mathbf{J}^{(\mathrm{fl})}(\mathbf{r}',\omega), & \mathbf{r}' \in V_{\mathrm{therm}}, \end{cases}$$
(2)

where V_{therm} is the volume occupied by the thermal objects and $V_{\rm ref}$ is the domain occupied by the nonabsorbing background reference medium characterized by a purely real dielectric function $\varepsilon_{\rm ref}(\omega)$. The fluctuating electric current density ${\bf J}^{\rm (fl)}({\bf r}',\omega)$ arises from the thermal excitation of microcharges and is defined in terms of its autocorrelation function via the fluctuation-dissipation theorem as⁶²

$$\langle \mathbf{J}^{(\mathrm{fl})}(\mathbf{r},\omega)\mathbf{J}^{(\mathrm{fl})^{\dagger}}(\mathbf{r}',\omega')\rangle = 4\pi\omega\varepsilon_{0}\mathrm{Im}[\varepsilon(\mathbf{r},\omega)]\Theta(\omega,T)\delta(\mathbf{r}-\mathbf{r}')\delta(\omega-\omega')\bar{\bar{\mathbf{I}}},$$
(3)

where \dagger specifies the conjugate transpose, ε_0 is the vacuum permittivity, and δ is the Dirac delta function. The mean energy of an electromagnetic state at temperature T and frequency ω is given by $\Theta(\omega, T) = \hbar\omega \left(e^{\frac{\hbar\omega}{k_BT}} - 1\right)^{-1}$, where \hbar is the reduced Planck constant and k_B is the Boltzmann constant.

The system Green's function $\overline{\overline{\mathbf{G}}}(\mathbf{r},\mathbf{r}',\omega)$ in Eq. (1) is defined from the self-consistent Green's function equation ⁵⁸

$$\overline{\overline{\mathbf{G}}}^{0}(\mathbf{r}, \mathbf{r}', \omega) = \overline{\overline{\mathbf{G}}}(\mathbf{r}, \mathbf{r}', \omega)
- k_{0}^{2} \int_{V_{\text{therm}}} \overline{\overline{\mathbf{G}}}^{0}(\mathbf{r}, \mathbf{r}'', \omega) \varepsilon_{\mathbf{r}}(\mathbf{r}'', \omega) \overline{\overline{\mathbf{G}}}(\mathbf{r}'', \mathbf{r}', \omega) d^{3}\mathbf{r}'',$$

where $k_0 = \omega \sqrt{\mu_0 \varepsilon_0}$ is the magnitude of the vacuum wavevector and the relative dielectric function is expanded as $\varepsilon_{\rm r}({\bf r},\omega) = \varepsilon({\bf r},\omega) - \varepsilon_{\rm ref}(\omega)$, with $\varepsilon({\bf r},\omega)$ being the dielectric function of the thermal objects. The free-space Green's function $\overline{\overline{\bf G}}^0({\bf r},{\bf r}',\omega)$ for ${\bf r}'\neq {\bf r}$ has known analytical solution

$$\overline{\overline{\mathbf{G}}}^{0}(\mathbf{r}, \mathbf{r}', \omega) = \frac{\exp(irk_{\text{ref}})}{4\pi r} \left[\left(1 - \frac{1}{(rk_{\text{ref}})^{2}} + \frac{i}{rk_{\text{ref}}} \right) \overline{\overline{\mathbf{I}}} - \left(1 - \frac{3}{(rk_{\text{ref}})^{2}} + \frac{3i}{rk_{\text{ref}}} \right) (\hat{\mathbf{r}}\hat{\mathbf{r}}^{\dagger}) \right], \tag{5}$$

where $r=|\mathbf{r}-\mathbf{r}'|$, $\hat{\mathbf{r}}=\frac{(\mathbf{r}-\mathbf{r}')}{|\mathbf{r}-\mathbf{r}'|}$, and $k_{\rm ref}=\omega\sqrt{\varepsilon_{\rm ref}(\omega)\varepsilon_0\mu_0}$. When $\mathbf{r}'=\mathbf{r}$, the analytical expression for the free-space dyadic Green's function has a singularity and must be solved using principal value techniques. Green's function is defined with respect to a vanishingly small exclusion volume around the singularity point. An additional term must then be added to the free-space Green's function to account for depolarization by the excluded volume. As we shall see, it is this treatment of the free-space Green's function at the source point $\mathbf{r}'=\mathbf{r}$ that is important in defining solutions for nonspherical dipole geometries.

C. Near-field energy density calculations

Near-field thermal emission from metasurfaces is characterized by the spectral energy density at an observation point above the metasurface. The spectral energy density above a metasurface at location ${\bf r}$ within the background reference medium is defined as 65,66

$$u(\mathbf{r},\omega) = \frac{\varepsilon_{\text{ref}}\varepsilon_0}{2} \langle \mathbf{E}(\mathbf{r},\omega) \cdot \mathbf{E}^*(\mathbf{r},\omega) \rangle + \frac{\mu_{\text{ref}}\mu_0}{2} \langle \mathbf{H}(\mathbf{r},\omega) \cdot \mathbf{H}^*(\mathbf{r},\omega) \rangle,$$
(6)

where represents the dot product, the superscript * is the complex conjugate, and $\mu_{\rm ref}$ is the relative permeability of the background reference medium. In this paper, we focus on modeling SiC, a material for which the magnetic contribution to the energy density is negligible in the dipole limit. ⁶⁷ As such, only the electric contribution to the energy density given by the first term on the right-hand side of Eq. (6) is maintained in the following equations.

Substituting in the expression for the electric field given by Eq. (1) and simplifying, the energy density generated by a system of thermal objects may be expressed as

$$u(\mathbf{r},\omega) = \frac{\varepsilon_{\text{ref}} k_0^4}{\omega} \int_{V_{\text{therm}}} \text{Tr} \left\{ \overline{\overline{\mathbf{G}}} \left(\mathbf{r}, \mathbf{r}', \omega \right) \left[\overline{\overline{\mathbf{G}}} (\mathbf{r}, \mathbf{r}', \omega) \right]^{\dagger} \right\} \text{Im} \left[\varepsilon(\mathbf{r}', \omega) \right] \Theta(\omega, T) d^3 \mathbf{r}'.$$
(7)

For a single dipole or a metasurface constructed of N thermal objects modeled as dipoles, Eq. (7) takes the discrete form

$$u(\mathbf{r},\omega) = \frac{\varepsilon_{\text{ref}} k_0^4}{\omega} \sum_{j}^{N} \Delta V_j \text{Tr} \left\{ \overline{\overline{\mathbf{G}}}(\mathbf{r}, \mathbf{r}_j, \omega) \left[\overline{\overline{\mathbf{G}}}(\mathbf{r}, \mathbf{r}_j, \omega) \right]^{\dagger} \right\} \times \text{Im}[\varepsilon(\mathbf{r}_j, \omega)] \Theta[\omega, T(\mathbf{r}_j)],$$
(8)

where ΔV_j is the volume of the jth dipole. Here, $\overline{\overline{\mathbf{G}}}(\mathbf{r}, \mathbf{r}_j, \omega)$ is the system Green's function relating the location \mathbf{r} at which energy density is calculated with the center-of-mass location \mathbf{r}_j of the jth dipole. This system Green's function $\overline{\overline{\mathbf{G}}}(\mathbf{r}, \mathbf{r}_j, \omega)$ is the main defining parameter of near-field thermal emission from a system of dipoles and is found by discretizing Eq. (4) over the second location coordinate as

$$\overline{\overline{\mathbf{G}}}(\mathbf{r}, \mathbf{r}_{j}, \omega) = \overline{\overline{\mathbf{G}}}^{0}(\mathbf{r}, \mathbf{r}_{j}, \omega) + k_{0}^{2} \sum_{k}^{N} \Delta V_{k} \varepsilon_{\mathbf{r}}(\mathbf{r}_{k}, \omega) \overline{\overline{\mathbf{G}}}^{0}(\mathbf{r}, \mathbf{r}_{k}, \omega) \overline{\overline{\mathbf{G}}}(\mathbf{r}_{k}, \mathbf{r}_{j}, \omega).$$
(9)

The discretized free-space Green's function $\overline{\overline{\mathbf{G}}}^{0}(\mathbf{r}, \mathbf{r}_{j}, \omega)$ found in both terms on the right-hand side of Eq. (9) may be represented analytically as⁶⁸

$$\overline{\overline{\mathbf{G}}}^{0}(\mathbf{r}, \mathbf{r}_{j}, \omega) = \frac{\exp(ir_{\mathbf{r}j}k_{\mathrm{ref}})}{4\pi r_{\mathbf{r}j}} \left[\left(1 - \frac{1}{(r_{\mathbf{r}j}k_{\mathrm{ref}})^{2}} + \frac{i}{r_{\mathbf{r}j}k_{\mathrm{ref}}} \right) \overline{\mathbf{I}} - \left(1 - \frac{3}{(r_{\mathbf{r}j}k_{\mathrm{ref}})^{2}} + \frac{3i}{r_{\mathbf{r}j}k_{\mathrm{ref}}} \right) \left(\hat{\mathbf{r}}_{\mathbf{r}j}\hat{\mathbf{r}}_{\mathbf{r}j}^{\dagger} \right) \right], \tag{10}$$

where $r_{rj} = |\mathbf{r} - \mathbf{r}_j|$ and $\hat{\mathbf{r}}_{rj} = \frac{(\mathbf{r} - \mathbf{r}_j)}{|\mathbf{r} - \mathbf{r}_j|}$. Equation (10) does not have any singularities since the location r at which energy density is calculated is outside of the thermal object domain and in the background reference medium (i.e., \mathbf{r} and \mathbf{r}_i are never equal).

The discrete system Green's function $\overline{\overline{\mathbf{G}}}(\mathbf{r}_k, \mathbf{r}_i, \omega)$ given in the second term on the right-hand side of Eq. (9) describes the interaction among all dipoles. $\overline{\mathbf{G}}(\mathbf{r}_k, \mathbf{r}_i, \omega)$ is calculated here using the method outlined in Ref. 58 with a special form for the self-term of the free-space Green's function to account for the ellipsoidal geometry of dipoles. To reduce computational costs in calculating $\overline{\mathbf{G}}(\mathbf{r}_k, \mathbf{r}_i, \omega)$, we implement the weak form⁶⁹ of the free-space Green's function self-term for ellipsoidal dipoles of variable rotation, given as

$$\overline{\overline{\mathbf{G}}}^{0}(\mathbf{r}_{i}, \mathbf{r}_{i}, \omega) = -\frac{\mathbf{A}^{-1}\overline{\overline{\mathbf{L}}}\mathbf{A}}{\Delta V_{i}k_{\text{ref}}^{2}},$$
(11)

where \mathbf{r}_i is the location of the center of mass of the *i*th dipole. The total rotation matrix $\mathbf{A} = \mathbf{R}_x \mathbf{R}_y \mathbf{R}_z$ accounts for rotation of the ellipsoidal dipoles from their local coordinate system by angles θ_x , θ_y , and θ_z around the x-, y-, and z-axes, respectively [see Fig. 1(a)]. The individual rotation matrices \mathbf{R}_x , \mathbf{R}_y , and \mathbf{R}_z are expanded as

$$\mathbf{R}_{x} = \begin{bmatrix} 1 & 0 & 0\\ 0 & \cos\theta_{x} & -\sin\theta_{x}\\ 0 & \sin\theta_{x} & \cos\theta_{x} \end{bmatrix}, \tag{12}$$

$$\mathbf{R}_{y} = \begin{bmatrix} \cos\theta_{y} & 0 & \sin\theta_{y} \\ 0 & 1 & 0 \\ -\sin\theta_{y} & 0 & \cos\theta_{y} \end{bmatrix}, \tag{13}$$

$$\mathbf{R}_{z} = \begin{bmatrix} \cos\theta_{z} & -\sin\theta_{z} & 0\\ \sin\theta_{z} & \cos\theta_{z} & 0\\ 0 & 0 & 1 \end{bmatrix}. \tag{14}$$

 $\mathbf{R}_z = \begin{bmatrix} \cos\theta_z & -\sin\theta_z & 0\\ \sin\theta_z & \cos\theta_z & 0\\ 0 & 0 & 1 \end{bmatrix}. \tag{14}$ The dyad $\overline{\mathbf{L}} = \begin{bmatrix} L_1 & 0 & 0\\ 0 & L_2 & 0\\ 0 & 0 & L_3 \end{bmatrix}$ accounts for the depolarization

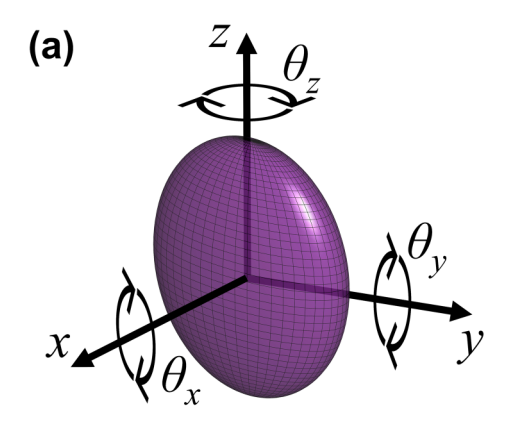
of ellipsoidal dipoles and has components^{64,70}

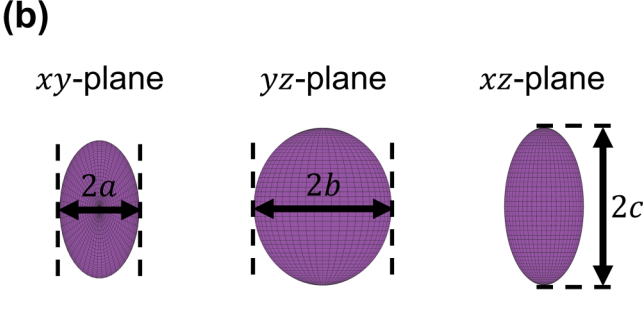
$$L_1 = \frac{abc}{2} \int_0^\infty (a^2 + q)^{-1} [(q + a^2)(q + b^2)(q + c^2)]^{-1/2} dq, \qquad (15)$$

$$L_2 = \frac{abc}{2} \int_0^\infty (b^2 + q)^{-1} [(q + a^2)(q + b^2)(q + c^2)]^{-1/2} dq, \qquad (16)$$

$$L_3 = \frac{abc}{2} \int_0^\infty (c^2 + q)^{-1} [(q + a^2)(q + b^2)(q + c^2)]^{-1/2} dq.$$
 (17)

These geometrical factors L_1 , L_2 , and L_3 are used in calculating the polarizability tensor of ellipsoidal dipoles in standard lightscattering theory. As such, Eqs. (15)-(17) may be applied to





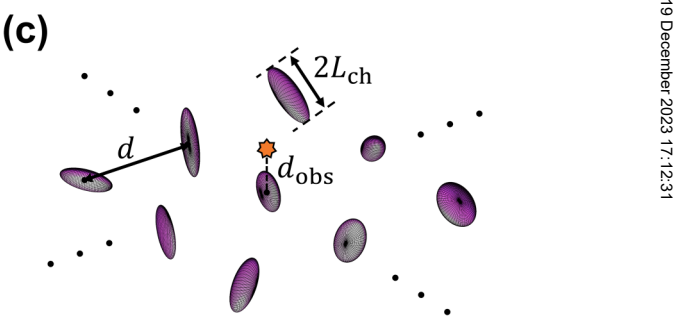


FIG. 1. (a) Ellipsoidal particle in its local coordinate system with rotation convention depicted. (b) The three major semiaxis dimensions of the ellipsoidal particle from panel (a). (c) Metasurface composed of a single layer of ellipsoidal particles. The observation point at which energy density is calculated is depicted by the yellow star and is located directly above the central particle in the 25-by-25 array.

define the polarizability of ellipsoidal dipoles in many-body models of near-field radiative heat transfer.

III. RESULTS AND DISCUSSION

A. System description

We model the near-field spectral energy density above single ellipsoidal particles and above metasurfaces formed from a 25-by-25 array of ellipsoidal particles. Energy density is calculated at a

distance d_{obs} along the vertical z-axis from the center of mass of single-particle systems and above the center of mass of the central particle in metasurfaces [see Fig. 1(c)]. For the metasurfaces, we model two different center-of-mass interparticle spacing values that are consistent with the assumptions for dipole approximations: $d = 3L_{\rm ch}$ (main paper) and $d = 6L_{\rm ch}$ (supplementary material).

All particles are made of SiC, supporting LSPhs in the infrared spectral band. The particles are embedded in a nonabsorbing medium with dielectric function $\varepsilon_{ref}=3$. The value of $\varepsilon_{ref}=3$ was used because it leads to an increase in near-field thermal energy density from SiC particles as compared with SiC particles embedded in vacuum. 50 The particle interactions with any interfaces of the host medium are neglected. The dielectric function of SiC is calculated using a Lorentz oscillator model (see supplementary material, Sec. S1).

Each particle in a system is set to room temperature (T = 300 K) and is of volume $\Delta V_j = (4/3)\pi R_{\text{eq}}^3$, where $R_{\text{eq}} = 35 \text{ nm}$ is the radius of a sphere of equivalent volume. All particles are restricted to radial values $10 \text{ nm} \le \{a, b, c\} \le 100 \text{ nm}$. This range was chosen because the weak form of the free-space Green's function given in Eq. (11) does not deviate significantly from the more accurate strong form for these particle sizes. Therefore, we may model thermal emission using the weak form of the free-space Green's function, thereby decreasing computational loads without loss of accuracy.

B. Single particles of variable dimensions

To act as a reference for subsequent metasurface calculations, we first model the energy density above single ellipsoidal particles of variable dimensions. Sphericity Ψ is used to quantify the dimensions of an ellipsoid by a single representative value. Sphericity is defined as the ratio of the surface area of the ellipsoidal particle $A_{\text{ellipsoid}}$ to the surface area of a sphere of equivalent volume A_{sphere} ,

$$\Psi = \frac{A_{\text{ellipsoid}}}{A_{\text{sphere}}}.$$
 (18)

For a given sphericity value, there are 3! = 6 possible ellipsoid realizations that arise from permutation of the three distinct ellipsoid semiaxes a, b, and c.

For these single-particle simulations, we calculate the spectral energy density at a distance $d_{\rm obs}=2L_{\rm ch}$ above the center of mass of each ellipsoidal particle. Five different sphericity values are considered for ellipsoidal particles, $\Psi = 0.54083$, 0.69050, 0.83094, 0.916 93, 0.989 26 [Figs. 2(a)-2(e)], and the resulting spectral energy densities are compared with that of a perfectly spherical particle of $\Psi = 1$ [Fig. 2(f)]. For reference, we also calculate the total energy density above 55 different particles of unique sphericity ranging from $0.540\,83 \le \Psi \le 1$ (see supplementary material, Sec. S2). The lower sphericity limit $\Psi = 0.540\,83$ arises from the condition that all particles are of the same volume and the requirement that the semiaxis lengths are in the range $10 \text{ nm} \le \{a, b, c\} \le 100 \text{ nm}$.

For the six geometric permutations of particles at a given sphericity value, there are only three unique spectra of energy density at the chosen observation point [Figs. 2(a)-2(e)]. The degeneracy of the spectra arises from geometric permutations that correspond to a rotation around the z-axis (e.g., $\{a, b, c\}$ and $\{b, a, c\}$). This degeneracy is expected to disappear when the energy density is calculated at a point that does not lie along an axis of symmetry for the ellipsoidal particle.

The three resonances in the spectral energy density of ellipsoidal particles arise from shape-dependent LSPhs. 70 LSPhs exist in the Reststrahlen spectral band in which the real part of the dielectric function is negative. For SiC, the Reststrahlen band is defined between the transverse optical and longitudinal optical phonon frequencies, $\omega_{TO} = 1.494 \times 10^{14}$ and $\omega_{LO} = 1.824 \times 10^{14} \text{ rad/s}$, respectively. Tuning the thermal energy density of SiC particles through geometric alteration is restricted to this frequency range. For ellipsoidal particles, the three unique LSPh resonances correspond to the three unique semiaxes a, b, and c that define the geometry of an ellipsoid surface. In general, the number of LSPh resonances decreases with increasing particle symmetry. For instance, spheroids have two unique semiaxis and therefore support two unique LSPh resonances, whereas spheres only have one unique radial value and support one unique LSPh resonance. The exact location, magnitude, and width of these resonances, however, are more complicated functions of material parameters.

In addition to the particle shape, the frequencies at which LSPh resonances occur (ω_{LSPh}) are dependent on the dielectric function of the particles and the dielectric function of the background reference medium and can be approximated from the relation

$$\varepsilon(\omega_{\rm LSPh}) = \varepsilon_{\rm ref} \left(1 - \frac{1}{L_i} \right),$$
 (19)

 $\varepsilon(\omega_{\rm LSPh}) = \varepsilon_{\rm ref} \left(1 - \frac{1}{L_i} \right), \tag{19}$ where L_i refers to the geometrical factors given in Eqs. (15)–(17). Ξ This relation is valid for particles in the dipole limit and is derived from standard electromagnetic contrains the second Ξ . from standard electromagnetic scattering theory by determining $\frac{1}{12}$ the poles in the polarizability tensor function of ellipsoidal dipoles. Prediction of resonance frequencies for SiC ellipsoidal particles of variable sphericity is given in Sec. S3 of the supplementary material through solution of Eq. (19) for $\varepsilon_{\rm ref}=$ 3. These predicted frequencies agree with the location of resonances in the spectral energy density of the corresponding single-particle systems presented in Figs. 2(a)-2(f), illustrating that near-field thermal emission is dominated by LSPhs. Note that the dielectric function of the background reference medium has a noticeable impact on LSPh resonances. For instance, the LSPh resonance of SiC spherical particles blueshifts from 1.677×10^{14} to 1.754×10^{14} rad/s when $\varepsilon_{\rm ref}$ varies from 3 to 1.

In these single-particle systems, the range over which the LSPh resonances occur tends to shrink as particle sphericity increases, eventually becoming a single resonance for spherical particles (see supplementary material, Sec. S3, Fig. S3). The same trends are seen in the spectral energy density above single particles [Figs. 2(a)–2(f)]. For the least spherical particle [i.e., $\Psi = 0.540\,83$, see Fig. 2(a)], the peak-to-peak range of the resonances in the spectral energy density is 2.4024 × 10¹³ rad/s. This range is over 5.7 times that of the peak-to-peak range $(4.154 \times 10^{12} \text{ rad/s})$ of the ellipsoidal particle with the highest sphericity [i.e., $\Psi = 0.98926$, see Fig. 2(e)]. As such, the bandwidth of near-field thermal

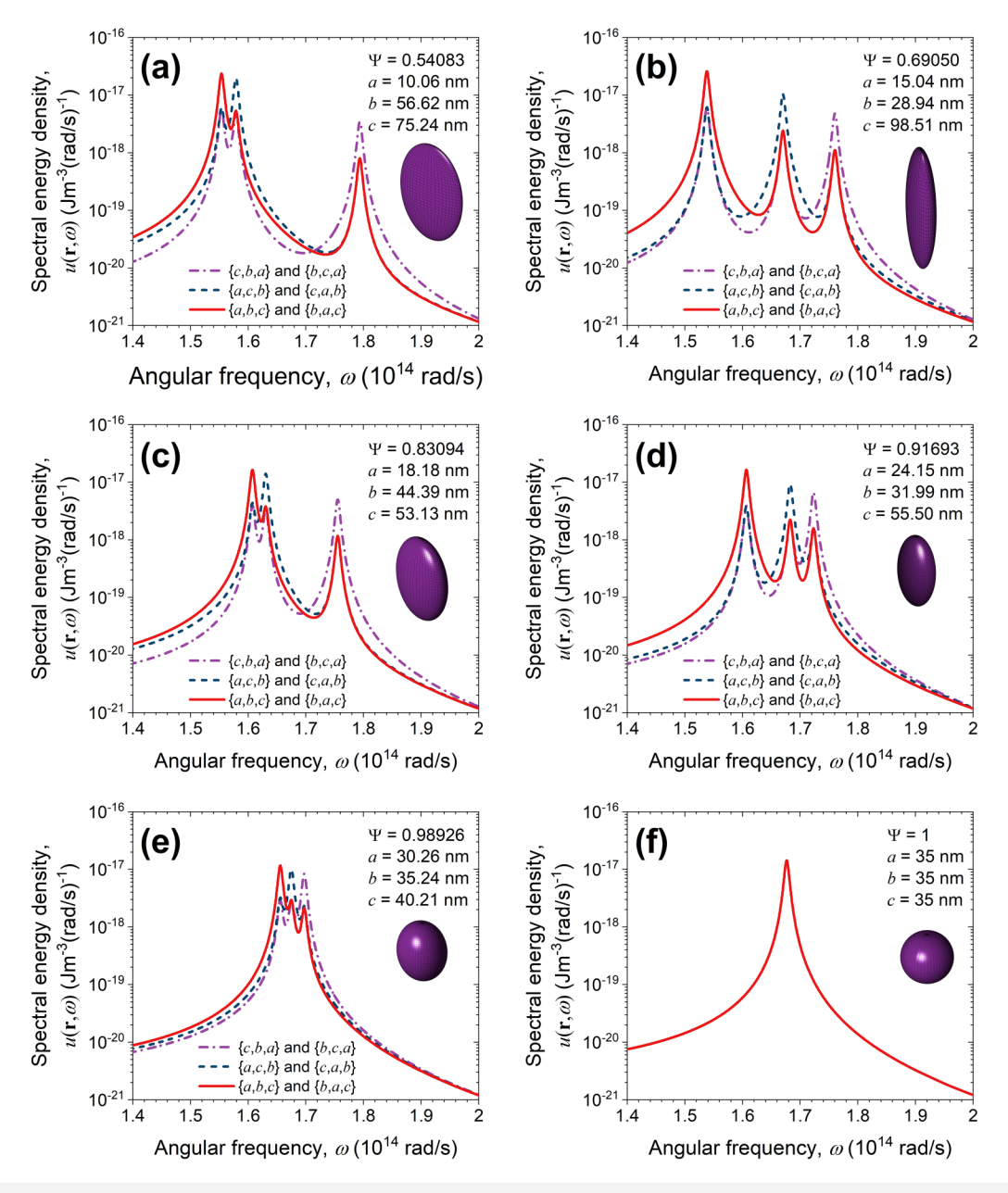


FIG. 2. Spectral energy density above a single particle of variable sphericity: (a)–(e) ellipsoidal particles, (f) spherical particle. All particles are SiC, at temperature $T=300\,\mathrm{K}$, and embedded in a nonabsorbing background medium of $\varepsilon_{\mathrm{ref}}=3$. Each sphericity value corresponds to six geometric permutations of the ellipsoidal particles, represented by sets in curly brackets [panels (a)–(e)]. Particles are unrotated such that the particle center of mass is set at the origin and the three major ellipsoid semiaxes are aligned with the axes of the Cartesian coordinate system. The observation point is located at a vertical distance of $d_{\mathrm{obs}}=2L_{\mathrm{ch}}$ above each particle along the zaxis

emission may be decreased by changing the particle geometry to more spherical forms. For single particles, the application space for such tuning functionality is limited. To provide a more practical example, we next model metasurfaces composed of many ellipsoidal particles.

C. Metasurfaces with constituent particles of variable dimensions

Next, we model six different metasurfaces with constituent particles of variable sphericity and compare the resulting spectra to

that of single-particle systems. All particles within a given metasurface are of the same dimensions and orientation, and particle sphericity is chosen to be consistent with that modeled in the single-particle systems of Sec. III B (i.e., $\Psi = 0.54083$, 0.69050, 0.830 94, 0.916 93, 0.989 26, 1). While we present results for observation points at $d_{obs} = 2L_{ch}$, a similar spectral behavior is seen for farther observation points tested at $d_{obs} = 7L_{ch}$ (not shown).

The spectral behavior of thermal emission from metasurfaces with close interparticle spacing [i.e., $d = 3L_{ch}$, see Figs. 3(a)-3(f)] is found to deviate from that of individual constituent particles. Specifically, the maximum absolute value of the relative

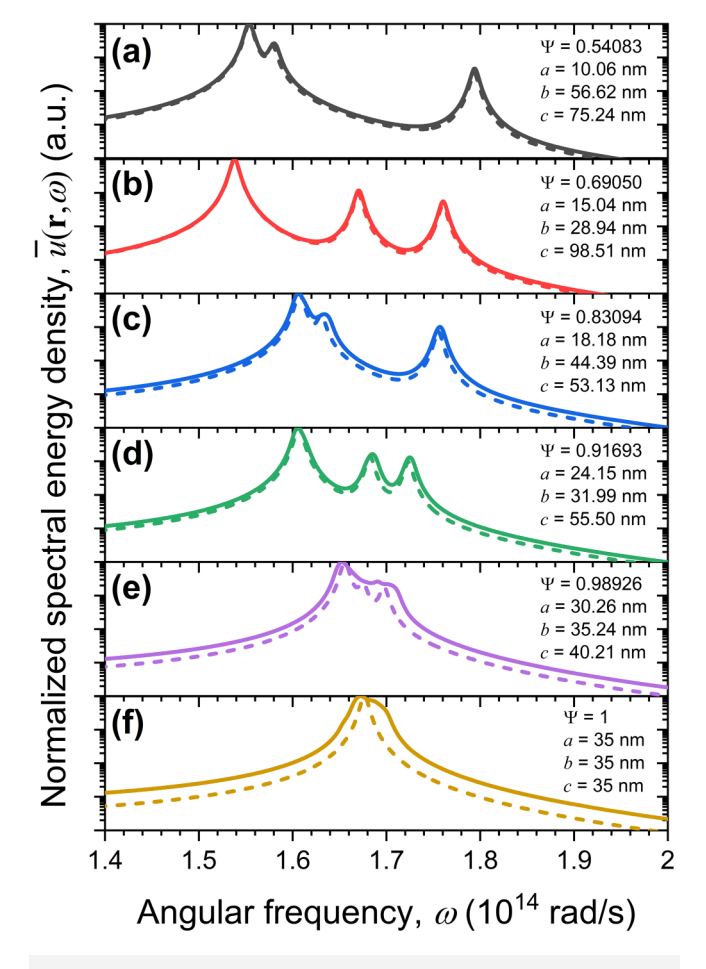


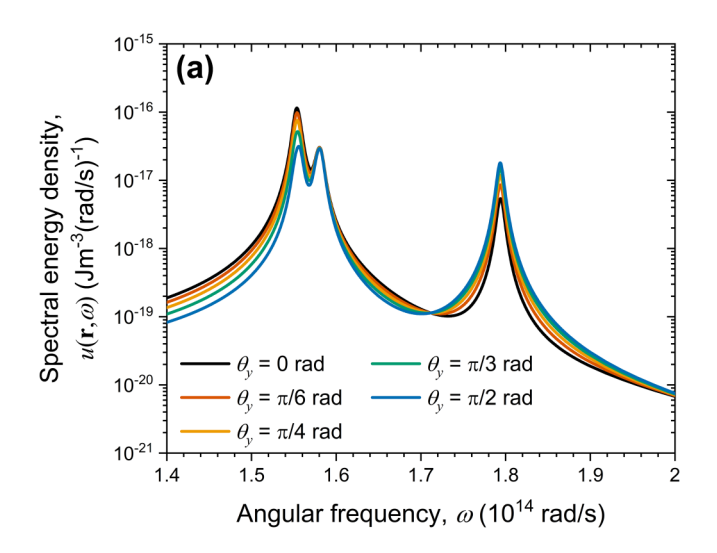
FIG. 3. Normalized spectral energy density above metasurfaces with constituent particles of variable sphericity: (a)-(e) ellipsoidal particles, (f) spherical particles. Normalization is implemented as $\bar{u}(\mathbf{r}, \omega) = u(\mathbf{r}, \omega)/\text{max}[u(\mathbf{r}, \omega)]$ for each system. Each metasurface is composed of a 25-by-25 array of ellipsoidal SiC particles at temperature $T = 300 \, \text{K}$ and embedded in a nonabsorbing background medium of $\varepsilon_{ref}=3$. Solid lines represent metasurfaces and dashed lines represent a single particle. The sphericity of each particle is varied from $\Psi = 0.540\,83$ to $\Psi = 1$. All particles are unrotated. Interparticle spacing is $d=3L_{\rm ch}$. The observation point is located at a vertical distance of $d_{\rm obs}=2L_{\rm ch}$ above the center of mass of the central particle in the array.

difference between the normalized energy density spectra of a metasurface and the corresponding individual particle (i.e., $\max[|\bar{u}_{metasurface}(\mathbf{r}, \omega) - \bar{u}_{particle}(\mathbf{r}, \omega)|/\bar{u}_{particle}(\mathbf{r}, \omega)])$ is between 42% and 941% over the Reststrahlen band for all metasurfaces modeled. Conversely, the spectrum of thermal emission from metasurfaces with larger interparticle spacing [i.e., $d = 6L_{ch}$, see supplementary material, Sec. S4, Figs. S5(a)-S5(f)] is found to be approximated to a high degree of accuracy by that of individual constituent particles (i.e., $\max[|\bar{u}_{\text{metasurface}}(\mathbf{r}, \omega) - \bar{u}_{\text{particle}}(\mathbf{r}, \omega)|/\bar{u}_{\text{particle}}(\mathbf{r}, \omega)] \lesssim 21\%$ over the Reststrahlen band for all metasurfaces modeled). These trends have been observed for arrays of spherical dipoles⁵⁰ and may be attributed to the degree of multiparticle interaction within a metasurface. 71,72 In the metasurfaces with close interparticle spacing $d = 3L_{ch}$, multiparticle interaction significantly influences the near-field spectral energy density. This contribution may be seen from the relative value of off-diagonal terms in the discrete system Green's function $\overline{\mathbf{G}}(\mathbf{r}_k, \mathbf{r}_i, \omega)$ that describes the interaction between all particles in a metasurface (see supplementary material, Sec. S5). For metasurfaces with close interparticle spacing $d = 3L_{ch}$, the off-diagonal terms of $\overline{\mathbf{G}}(\mathbf{r}_k, \mathbf{r}_i, \omega)$ are relatively large, indicating significant multiparticle interaction [see supplementary material, Sec. S5, Figs. S6(a)-S6(b)]. As the interparticle spacing is increased, however, the discrete system Green's function $\overline{\mathbf{G}}(\mathbf{r}_k, \mathbf{r}_i, \omega)$ becomes increasingly diagonal [see supplementary material, Sec. S5, Figs. S6(c)-S6(d)], signifying that individual particle self-interaction dominates, multiparticle interactions are negligible, and the spectral energy density of the metasurface may be approximated as the linear computation spectral energy density values of constituent particles. Interestingly, the phenomenon described in this paragraph is similar to the similar deflect in field emission, where field enhances in an emitter of the similar deflect. ment can be modulated by changing the spacing in an emitter array.

A similar analysis may be used to explain why the spectra of 3 metasurfaces composed of less spherical particles (i.e., small Ψ) more closely match the corresponding single-particle spectra even when the metasurface has closer interparticle spacing $d = 3L_{ch}$ [Figs. 3(a)-3(f)]. This trend can be seen explicitly when comparing the spectra of the highest sphericity $[\Psi = 1, Fig. 3(f)]$ and lowest sphericity $[\Psi = 0.540 \, 83, \, \text{Fig. 3(a)}]$ systems. The maximum relative difference in the spectra of metasurfaces vs single particles with $d = 3L_{\rm ch}$ and $\Psi = 1$ [Fig. 3(f)] is 941%, whereas this value is only 83% for metasurfaces and single particles with $d = 3L_{ch}$ and $\Psi = 0.540\,83$ [Fig. 3(a)]. Since the interparticle spacing is defined with respect to the characteristic length of constituent particles (i.e., $d = 3L_{ch}$) and less spherical particles have greater characteristic length values, the lower sphericity metasurfaces correspond to systems with larger interparticle spacing. As such, multiparticle interaction in these systems is less significant, and the spectra of these metasurfaces may be approximated by that of single particles.

D. Metasurfaces with constituent particles of variable orientation

Next, we model metasurfaces for which the constituent ellipsoidal particles are all rotated by the same angle θ_{ν} around the y-axis in the local coordinate system of every particle (Fig. 4). All local coordinate systems are parallel to the global Cartesian



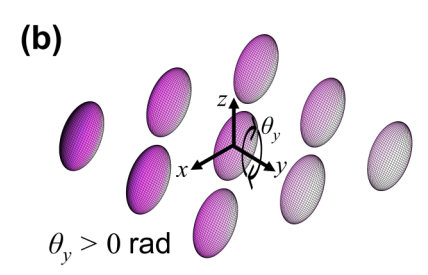


FIG. 4. (a) Spectral energy density above metasurfaces with constituent particles of variable rotation angle. Each metasurface is composed of a 25-by-25 array of ellipsoidal SiC particles at temperature $T=300\,\mathrm{K}$ and embedded in a nonabsorbing background medium of $\varepsilon_{\rm ref}=3$. (b) Particles are rotated by the same angle θ_{V} in their local coordinate system and are of the same dimensions (a = 10.06 nm, b = 56.62 nm, c = 75.24 nm, $\Psi = 0.540 \, 83$). Interparticle spacing is $d=3L_{\rm ch}$. The observation point is located at a vertical distance of $d_{\rm obs}$ = 2L_{ch} above the center of mass of the central particle in the array.

coordinate system. In the metasurface modeled, the constituent ellipsoidal particles are all the same dimensions (i.e., a = 10.06 nm, $b = 56.62 \text{ nm}, \quad c = 75.24 \text{ nm}, \quad \Psi = 0.540 \text{ 83}, \quad \text{and} \quad \text{interparticle}$ spacing is $d=3L_{\rm ch}$. Energy density is calculated at a distance $d_{\rm obs} = 2L_{\rm ch}$ above the center of mass of the central particle. The spectral profile at the observation point $d_{\rm obs}=2L_{\rm ch}$ is consistent with the spectra at farther separation distances (e.g., $d_{\rm obs} = 7L_{\rm ch}$, not shown), with only differences in magnitude.

Rotation of all particles in the array results in damping of the low-frequency resonance at $1.554\times10^{14}\,\text{rad/s}$, amplification of the high-frequency resonance at 1.794 × 10¹⁴ rad/s, and minimal change in the middle resonance at 1.579×10^{14} rad/s [Fig. 4(a)]. There is a negligible spectral shift in resonances with a change in ellipsoid orientation. This independence of particle orientation and resonance location is expected in the regime in which multiparticle interaction effects are less significant. Based on the results in Fig. 3(a) that compare an equivalent unrotated metasurface with a single particle, we can assume that we are in this regime where

individual particle self-interaction dominates. While different in magnitude, the spectral profile of energy density for the metasurfaces with particles at $\theta_v = 0$ rad [black line, Fig. 4(a)] and $\theta_v = \pi/2$ rad/s [blue line, Fig. 4(a)] match, respectively, the single-particle spectra for $\{a, b, c\}$ and $\{c, b, a\}$ particles of sphericity $\Psi = 0.54083$ in Fig. 2(a). These single-particle geometric permutations correspond to the same orientation as that of the constituent particles in the metasurface at, respectively, $\theta_{\nu} = 0$ rad and $\theta_{\nu} = \pi/2$ rad/s. As such, the spectral energy density of each of these metamaterials with similarly oriented particles should be well represented by a linear combination of single-particle spectra. The same conclusions are applicable when interparticle spacing is $d = 6L_{ch}$ (see supplementary material,

The total, spectrally integrated energy density at $\theta_{\nu} = 0$ rad is almost double that at $\theta_v = \pi/2 \text{ rad/s}$ (see supplementary material, Sec. S7). As such, metasurfaces like this one with dynamic control of the orientation of constituent particles could be implemented as thermal switches.

E. Metasurfaces with randomized constituent particles

Next, we introduce randomization into metasurfaces. Randomization is incorporated in three different ways: (1) random particle dimensions, (2) random particle orientation, and (3) both random particle dimensions and random particle orientation. In all random particle semiaxes are constraints systems, particle semiaxes are constraints $\leq 100 \, \text{nm}$ with a < b < c, and the particle characteristic length to defined as the maximum radial dimension over all particles in the defined as the maximum radial dimension over all particles in the defined as the maximum radial dimension over all particles in the defined as the maximum radial dimension over all particles in the defined as the maximum radial dimension over all particles in the defined as the maximum radial dimension over all particles in the defined as the maximum radial dimension over all particles in the defined as the maximum radial dimension over all particles in the defined as the maximum radial dimension over all particles in the defined as the maximum radial dimension over all particles in the defined as the maximum radial dimension over all particles in the defined as the maximum radial dimension over all particles in the defined as the maximum radial dimension over all particles in the defined as the maximum radial dimension over all particles in the defined as the maximum radial dimension over all particles in the defined as the defined as the maximum radial dimension over all particles in the defined as the defi tary material, Sec. S8) are modeled. The spectral energy density is calculated at six different distances above the central particle in each metasurface, from $d_{\rm obs} = 2L_{\rm ch}$ to $7L_{\rm ch}$.

In the random particle dimensions metasurfaces [Figs. 5(a)–5(b) $\frac{12}{50}$ and in the supplementary material, Sec. S8, Figs. S9(a)-S9(b)], particles are oriented as $\theta_x = \theta_y = \theta_z = 0$. The spectral energy density of these metasurface differs noticeably from all previous cases. Instead of three distinct resonances, the spectral energy density displays multiple resonances and becomes increasingly broadband at farther distances above the metasurface. Focusing on the metasurface with interparticle spacing $d = 3L_{ch}$, the spectral energy density has five main resonances at the observation point $d_{\rm obs} = 2L_{\rm ch}$. In this case, the location of the three dominant resonances may be predicted from the geometric parameters of the central particle in the 25-by-25 array above which the observation point is located. This spectral behavior is due to the dominance of the central particle in the array at very close observation points in addition to only minor multiparticle interaction effects. At farther observation points, the central particle in the metasurface becomes less dominant to thermal emission as the same solid angle from the observation point encompasses a larger number of particles. This same logic may be applied in interpreting the spectral energy density above the metasurface with interparticle spacing $d = 6L_{ch}$. This implies that it is critical to control particle dimensions to obtain narrowband thermal emission from metasurfaces made of dielectric particles. In all of these cases, the spectral energy density may be approximated as the summation of all single-particle spectra weighted by the distance from the

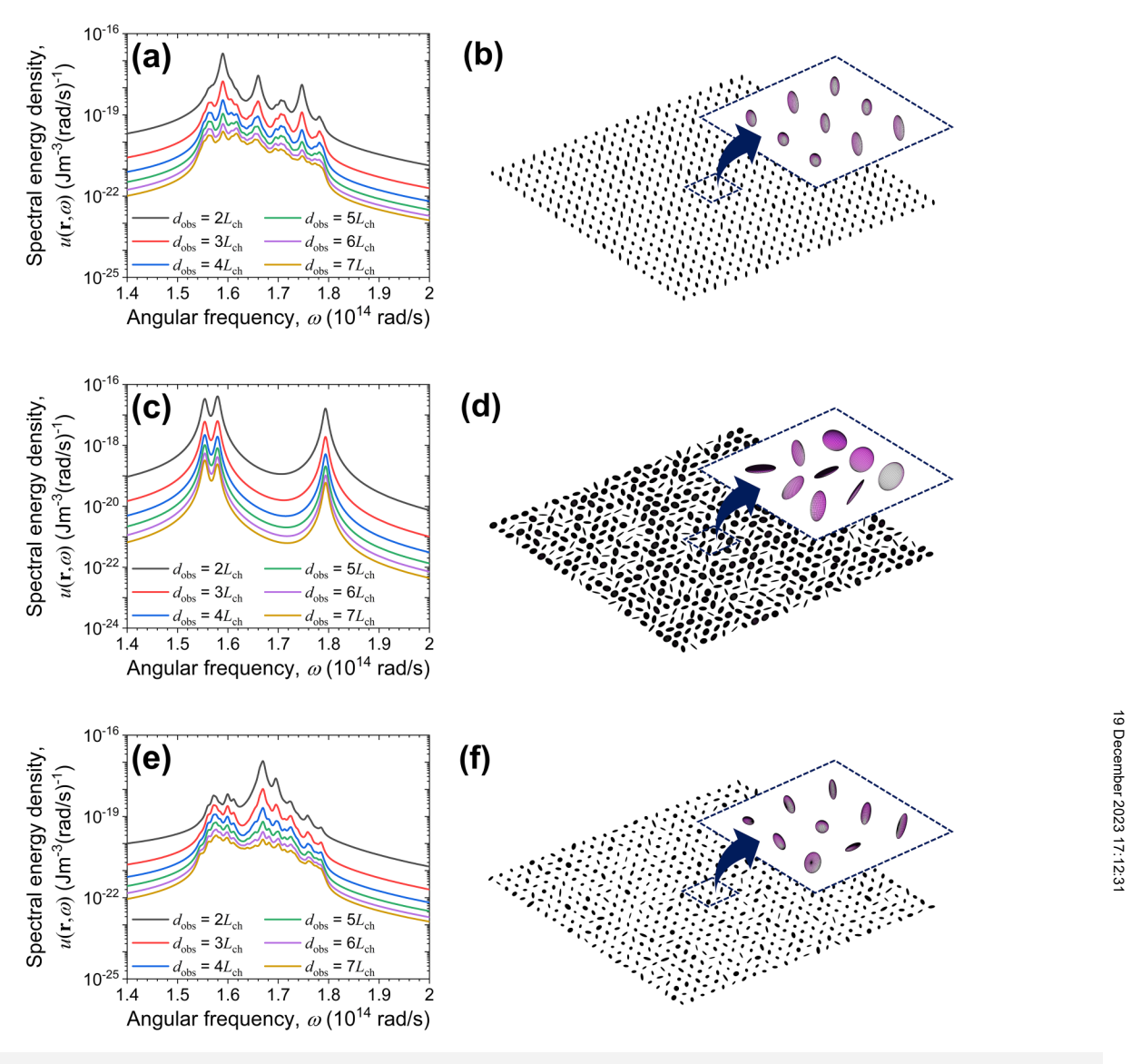


FIG. 5. Spectral energy density above metasurfaces with randomized constituent particles. Each metasurface is composed of a 25-by-25 array of ellipsoidal SiC particles at temperature $T=300\,\mathrm{K}$ and embedded in a nonabsorbing background medium of $\varepsilon_{\mathrm{ref}}=3$. (a) and (b) Particles are unrotated and of random dimensions; (c) and (d) particles are all the same dimensions ($a=10.06\,\mathrm{nm}$, $b=56.62\,\mathrm{nm}$, $c=75.24\,\mathrm{nm}$, $\Psi=0.5408$) and of random orientation; and (e) and (f) particles are of random dimensions and random orientation. Interparticle spacing is $d=3L_{\mathrm{ch}}$. Spectral energy density is measured at six different observation points located at vertical distances of $d_{\mathrm{obs}}=2L_{\mathrm{ch}}$, $3L_{\mathrm{ch}}$, $4L_{\mathrm{ch}}$, $5L_{\mathrm{ch}}$, $6L_{\mathrm{ch}}$, $7L_{\mathrm{ch}}$ above the center of mass of the central particle in the array.

individual particle to the observation point. This approximation will begin to deviate from actual thermal emission spectra when interparticle spacing is small enough that multiparticle interactions become important.

Next, we model a metasurface composed of randomly orientated particles of low-sphericity ellipsoids (i.e., $\Psi = 0.540\,83$) and random rotation angles θ_x , θ_y , and θ_z for each particle [Figs. 5(c) and 5(d) and in the supplementary material, Sec. S8, Figs. S9(c)–S9(d)]. As expected from the analysis in Sec. III D, randomizing the

orientation of constituent particles only results in a change in the magnitude of each resonance and does not affect the frequency location of resonances in the spectral energy density. At all observation points, the spectral energy density displays three clear resonances at the same frequencies as LSPh resonances of single-particle systems and nonrandomized metasurfaces constructed of particles of the same dimensions. Multiparticle interaction effects are inferred to be less significant. These results imply that tunable, narrowband thermal emission can be achieved

from metasurfaces made of dielectric particles dominated by individual particle self-interaction effects if the dimensions of constituent particles are well-controlled, irrespective of particle alignment.

Finally, we model a metasurface composed of particles with random dimensions and random orientations [Figs. 5(e) and 5(f) and in the supplementary material, Sec. S8, Figs. S9(e)–S9(f)]. The spectral energy density displays similar trends to that of the metasurface made of unrotated, randomly dimensioned particles: the spectral energy density from the metasurface can be approximated as a weighted sum of single-particle spectra, and the spectral energy density becomes increasingly broadband over the Reststrahlen band for farther observation points. These results lead us to expect that actual metasurfaces made of dielectric particles manufactured with nonperfect particle alignment and constructed of particles defined by size distributions rather than exact dimensions will display an averaging of LSPh resonances and more broadband spectra than idealized structures.

IV. CONCLUSIONS

We have presented an exact method for calculating near-field energy density from metasurfaces composed of ellipsoidal particles in the dipole limit. This method is derived using a variation of the discrete system Green's function method and can be applied to resolve unique trends in the spectral energy density at arbitrary observation points above particle-based metasurfaces. We applied this method to model a variety of metasurfaces composed of SiC ellipsoidal particles of variable dimensions and orientations. The main finding of this work is that the geometric parameters of constituent particles can be used to control the frequency and bandwidth of LSPh resonances, thereby providing tunability of the spectral energy density from dielectric particle-based metasurfaces. Metasurfaces with interparticle spacing larger than a few times the characteristic length of the constituent particles are dominated by individual particle self-interaction. As such, the spectral thermal emission of these metasurfaces may be approximated as a linear combination of individual-particle spectra. For metasurfaces with interparticle spacing below this limit, multiparticle interactions come into play, and full-system models are required to accurately resolve the spectral energy density. These results are important for characterizing dielectric particle-based metasurfaces that are constructed of particles defined by distributions of geometric parameters rather than exact values.

SUPPLEMENTARY MATERIAL

See the supplementary material for the dielectric function of SiC; total (spectrally integrated) energy density results; frequency prediction of LSPh resonances for ellipsoidal dipoles; visualization of a discrete system Green's function; and the spectral energy density results for metasurfaces with interparticle spacing of $d=6L_{\rm ch}$.

ACKNOWLEDGMENTS

The authors acknowledge financial support from the National Science Foundation (Grant Nos. CBET-1952210 and CMMI-2130083). L.P.W. acknowledges that this material is based

upon work supported by the National Science Foundation Graduate Research Fellowship under Grant No. DGE-1747505. Any opinions, findings, and conclusions or recommendations expressed in this material are those of the authors and do not necessarily reflect the views of the National Science Foundation. M.F. acknowledges the support of the Natural Sciences and Engineering Research Council of Canada (NSERC) (Funding Reference No. RGPIN-2023-03513).

AUTHOR DECLARATIONS

Conflict of Interest

The authors have no conflicts to disclose.

Author Contributions

Lindsay P. Walter: Conceptualization (equal); Formal analysis (lead); Investigation (lead); Methodology (lead); Software (lead); Validation (lead); Visualization (lead); Writing – original draft (lead). Joseph C. McKay: Conceptualization (supporting); Methodology (supporting); Writing – review & editing (equal). Bart Raeymaekers: Funding acquisition (equal); Supervision (supporting); Writing – review & editing (equal). Mathieu Francoeur: Conceptualization (equal); Data curation (lead); Funding acquisition (equal); Project administration (lead); Resources (lead); Supervision (lead); Writing – review & editing (lead).

DATA AVAILABILITY

The data that support the findings of this study are available from the corresponding authors upon reasonable request.

REFERENCES

¹W. Cai and V. Shalaev, *Optical Metamaterials: Fundamentals and Applications* (Springer Science+Business Media, New York, 2010).

²X. Liu, T. Tyler, T. Starr, A. F. Starr, N. M. Jokerst, and W. J. Padilla, Phys. Rev. Lett. **107**, 045901 (2011).

³A. Sakurai, K. Yada, T. Simomura, S. Ju, M. Kashiwagi, H. Okada, T. Nagao, K. Tsuda, and J. Shiomi, ACS Cent. Sci. 5, 319–326 (2019).

⁴A. Nagpal, M. Zhou, O. Ilic, Z. Yu, and H. A. Atwater, Opt. Express 31, 11227

⁵J.-J. Greffet, R. Carminati, K. Joulain, J.-P. Mulet, S. Mainguy, and Y. Chen, Nature **416**, 61–64 (2002).

⁶E. Sakr, S. Dhaka, and P. Bermel, Proc. SPIE 9743, 97431D (2016).

⁷Y. Tian, A. Ghanekar, M. Ricci, M. Hyde, O. Gregory, and Y. Zheng, Materials (Basel) 11, 862 (2018).

⁸S. Inampudi, J. Cheng, M. M. Salary, and H. Mosallaei, J. Opt. Soc. Am. B 35, 39 (2018).

⁹Y. Zhai, Y. Ma, S. N. David, D. Zhao, R. Lou, G. Tan, R. Yang, and X. Yin, Science 355, 1062–1066 (2017).

¹⁰G. Ulpiani, G. Ranzi, K. W. Shah, J. Feng, and M. Santamouris, Sol. Energy 209, 278–301 (2020).

¹¹S. Zeng, S. Pian, M. Su, Z. Wang, M. Wu, X. Liu, M. Chen, Y. Xiang, J. Wu, M. Zhang, Q. Cen, Y. Tang, X. Zhou, Z. Huang, R. Wang, A. Tunuhe, X. Sun, Z. Xia, M. Tian, M. Chen, X. Ma, L. Yang, J. Zhou, H. Zhou, Q. Yang, X. Li, Y. Ma, and G. Tao, Science 373, 692–696 (2021).

12V. Ercağlar, H. Hajian, I. D. Rukhlenko, and E. Ozbay, Appl. Phys. Lett. 121, 182201 (2022)

13 S. Fan and W. Li, Nat. Photonics 16, 182–190 (2022).

¹⁴S. Molesky, C. J. Dewalt, and Z. Jacob, Opt. Express 21, A96 (2013).

- ¹⁵P. N. Dyachenko, S. Molesky, A. Y. Petrov, M. Störmer, T. Krekeler, S. Lang, M. Ritter, Z. Jacob, and M. Eich, Nat. Commun. 7, 11809 (2016).
- ¹⁶D. N. Woolf, E. A. Kadlec, D. Bethke, A. D. Grine, J. J. Nogan, J. G. Cederberg, D. Bruce Burckel, T. S. Luk, E. A. Shaner, and J. M. Hensley, Optica 5, 213 (2018).
- ¹⁷M. Chirumamilla, G. V. Krishnamurthy, K. Knopp, T. Krekeler, M. Graf, D. Jalas, M. Ritter, M. Störmer, A. Y. Petrov, and M. Eich, Sci. Rep. 9, 1 (2019).
- ¹⁸H. Chalabi, A. Alù, and M. L. Brongersma, Phys. Rev. B **94**, 1 (2016).
- ¹⁹M. A. Kats, R. Blanchard, S. Zhang, P. Genevet, C. Ko, S. Ramanathan, and F. Capasso, Phys. Rev. X 3, 041004 (2013).
- ²⁰Y. Li, X. Bai, T. Yang, H. Luo, and C. W. Qiu, Nat. Commun. 9, 273 (2018).
- ²¹T. Kim, J.-Y. Bae, N. Lee, and H. H. Cho, Adv. Funct. Mater. 29, 1807319 (2019).
- ²²R. Hu, W. Xi, Y. Liu, K. Tang, J. Song, X. Luo, J. Wu, and C.-W. Qiu, Mater. Today 45, 120–141 (2021).
- ²³M. M. Salary and H. Mosallaei, J. Appl. Phys. **125**, 163107 (2019).
- ²⁴J. Li, B. Yu, and S. Shen, Phys. Rev. Lett. **124**, 137401 (2020).
- ²⁵A. C. Overvig, S. A. Mann, and A. Alù, Phys. Rev. X 11, 021050 (2021).
- 26Y. Li, W. Li, T. Han, X. Zheng, J. Li, B. Li, S. Fan, and C.-W. Qui, Nat. Rev. Mater. 6, 488–507 (2021).
- ²⁷X. Liu and Z. Zhang, ACS Photonics 2, 1320–1326 (2015).
- ²⁸J. Dai, S. A. Dyakov, S. I. Bozhevolnyi, and M. Yan, Phys. Rev. B **94**, 125431 (2016).
- ²⁹V. Fernández-Hurtado, F. J. García-Vidal, S. Fan, and J. C. Cuevas, Phys. Rev. Lett. **118**, 203901 (2017).
- 30D. Lu, A. Das, and W. Park, Opt. Express 25, 12999 (2017).
- ³¹N. Vongsoasup, M. Francoeur, and K. Hanamura, Int. J. Heat Mass Transf. 115, 326–332 (2017).
- 32J. Shen, X. Liu, and Y. Xuan, Phys. Rev. Appl. 10, 034029 (2018).
- ³³Z. Zheng, A. Wang, and Y. Xuan, J. Quant. Spectrosc. Radiat. Transf. 208, 86–95 (2018).
- 34Y. H. Kan, C. Y. Zhao, and Z. M. Zhang, Phys. Rev. B 99, 035433 (2019).
- 35 W. Jin, S. Molesky, Z. Lin, and A. W. Rodriguez, Phys. Rev. B 99, 041403(R) (2019)
- ³⁶A. Ghanekar, L. Lin, J. Su, H. Sun, and Y. Zheng, Opt. Express 23, A1129 (2015)
- 37A. Ghanekar, L. Lin, and Y. Zheng, Opt. Express 24, A868 (2016).
- ³⁸M. C. Larciprete, M. Centini, R. Li Voti, and C. Sibilia, J. Opt. Soc. Am. B **34**, 1459 (2017)
- ³⁹H. Salihoglu, Z. Li, and S. Shen, Appl. Phys. Lett. **121**, 241701 (2022).
- ⁴⁰M. Francoeur, S. Basu, and S. J. Petersen, Opt. Express **19**, 18774 (2011).
- ⁴¹S. J. Petersen, S. Basu, B. Raeymaekers, and M. Francoeur, J. Quant. Spectrosc. Radiat. Transf. **129**, 277–286 (2013).
- 42S. Edalatpour, Phys. Rev. E 99, 063308 (2019).
- ⁴³M. Prisbrey, J. Greenhall, F. Guevara Vasquez, and B. Raeymaekers, J. Appl. Phys. 121, 014302 (2017).
- 44J. Greenhall and B. Raeymaekers, Adv. Mater. Technol. 2, 1700122 (2017).

- 45 A. Felt and B. Raeymaekers, Addit. Manuf. Lett. 5, 100120 (2023).
- 46 J. Dong, J. Zhao, and L. Liu, Phys. Rev. B 95, 125411 (2017).
- 47R. Messina, M. Tschikin, S.-A. Biehs, and P. Ben-Abdallah, Phys. Rev. B 88, 104307 (2013).
- ⁴⁸E. Tervo, B. A. Cola, and Z. Zhang, *Annual Review Heat Transfer* (Begell House, Inc., 2020), pp. 131–166.
- ⁴⁹M. Luo, J. Dong, J. Zhao, L. Liu, and M. Antezza, Phys. Rev. B **99**, 134207 (2019)
- ⁵⁰E. Tervo, Z. Zhang, and B. Cola, Phys. Rev. Mater. 1, 015201 (2017).
- ⁵¹E. Tervo, M. Francoeur, B. Cola, and Z. Zhang, Phys. Rev. B 100, 205422 (2019).
- ⁵²M. Luo, J. Zhao, L. Liu, and M. Antezza, Phys. Rev. B **102**, 024203 (2020).
- 53M. Luo, J. Zhao, and M. Antezza, Appl. Phys. Lett. 117, 053901 (2020).
- ⁵⁴M. Nikbakht, Phys. Rev. B **96**, 125436 (2017).
- 55 R. Incardone, T. Emig, and M. Krüger, Europhys. Lett. 106, 41001 (2014).
- ⁵⁶M. Nikbakht, J. Appl. Phys. **116**, 094307 (2014).
- 57O. R. Choubdar and M. Nikbakht, J. Appl. Phys. 120, 144303 (2016).
- ⁵⁸L. P. Walter, E. J. Tervo, and M. Francoeur, *Phys. Rev. B* **106**, 195417 (2022).
- ⁵⁹L. P. Walter and M. Francoeur, Appl. Phys. Lett. **121**, 182206 (2022).
- ⁶⁰P. Ben-Abdallah, S.-A. Biehs, and K. Joulain, Phys. Rev. Lett. **107**, 114301 (2011).
- 61S.-A. Biehs, R. Messina, P. S. Venkataram, A. W. Rodriguez, J. C. Cuevas, and P. Ben-Abdallah, Rev. Mod. Phys. 93, 25009 (2021).
- ⁶²S. M. Rytov, Y. A. Kravtsov, and V. I. Tatarskii, *Principles of Statistical Radiophysics 3: Elements of Random Fields* (Springer-Verlag, Berlin, 1989).
- 63 J. van Bladel, IRE Trans. Antennas Propag. 9, 563–566 (1961).
- 64 A. D. Yaghjian, Proc. IEEE 68, 248-263 (1980).
- 65C. A. Balanis, Advanced Engineering Electromagnetics, 2nd ed. (John Wiley & Sons, Inc., Hoboken, NJ, 2012).
- ⁶⁶M. Francoeur, in *Handbook of Thermal Science Engineering*, edited by F. A. Kulacki (Springer International Publishing AG, 2017), pp. 1–43.
- ⁶⁷P.-O. Chapuis, M. Laroche, S. Volz, and J.-J. Greffet, Appl. Phys. Lett. 92, 201906 (2008).
- ⁶⁸L. Novotny and B. Hecht, *Principles of Nano-Optics* (Cambridge University Press, Cambridge, 2006).
- ⁶⁹ A. Lakhtakia, Int. J. Mod. Phys. C **03**, 583–603 (1992).
- ⁷⁰C. F. Bohren and D. R. Huffman, Absorption and Scattering of Light by Small Particles (John Wiley & Sons, Inc., New York, 1983).
- ⁷¹ A. Lagendijk and B. A. van Tiggelen, Phys. Rep. 270, 143–215 (1996).
- ⁷²M. I. Mishchenko, OSA Contin. 1, 243 (2018).
- ⁷³Y. W. Zhu, T. Yu, F. C. Cheong, X. J. Xu, C. T. Lim, V. B. C. Tan, J. T. L. Thong, and C. H. Sow, Nanotechnology 16, 88–92 (2005).
- ⁷⁴J. R. Harris, K. L. Jensen, D. A. Shiffler, and J. J. Petillo, Appl. Phys. Lett. **106**, 201603 (2015)
- 75D. Biswas and R. Rudra, Phys. Plasmas 25, 083105 (2018).
- ⁷⁶S. V. Filippov, F. F. Dall'Agnol, E. O. Popov, A. G. Kolosko, and T. A. de Assis, J. Vac. Sci. Technol., B 41, 010601 (2023).